A&A 673, A24 (2023)
https://doi.org/10.1051/0004-6361/202346279

Astronomy & Astrophysics

The chemistry of H_2NC in the interstellar medium and the role of the C + NH_3 reaction⋆

M. Agúndez[1], O. Roncero[1], N. Marcelino[2,3], C. Cabezas[1], B. Tercero[2,3], and J. Cernicharo[1]

[1] Instituto de Física Fundamental, CSIC, C/ Serrano 123, 28006 Madrid, Spain
e-mail: marcelino.agundez@csic.es; octavio.roncero@csic.es
[2] Observatorio Astronómico Nacional, IGN, Calle Alfonso XII 3, 28014 Madrid, Spain
[3] Observatorio de Yebes, IGN, Cerro de la Palera s/n, 19141 Yebes, Guadalajara, Spain

Received 28 February 2023 / Accepted 21 March 2023

ABSTRACT

We carried out an observational search for the recently discovered molecule H_2NC, and its more stable isomer H_2CN, toward eight cold dense clouds (L1544, L134N, TMC-2, Lupus-1A, L1489, TMC-1 NH_3, L1498, and L1641N) and two diffuse clouds (B0415+379 and B0355+508) in an attempt to constrain its abundance in different types of interstellar regions and shed light on its formation mechanism. We detected H_2NC in all but one of the cold dense clouds targeted, while H_2CN was only detected in five out of the eight clouds. The column densities derived for both H_2NC and H_2CN are in the range 10^{11}–10^{12} cm^{-2}, and the abundance ratio H_2NC/H_2CN varies between 0.51 and >2.7. The metastable isomer H_2NC is therefore widespread in cold dense clouds, where it is present with an abundance similar to that of H_2CN. We did not detect H_2NC or H_2CN in any of the two diffuse clouds targeted, meaning we can make no conclusions regarding how the chemistry of H_2NC and H_2CN varies between dense and diffuse clouds. We find that the column density of H_2NC is correlated with that of NH_3, which strongly suggests that these two molecules are chemically linked, ammonia most likely being a precursor of H_2NC through the C + NH_3 reaction. We performed electronic structure and statistical calculations that show that both H_2CN and H_2NC can be formed in the C + NH_3 reaction through two different channels involving two different transition states that are very close in energy. The predicted product branching ratio H_2NC/H_2CN is very method dependent, but values between 0.5 and 0.8 are the most likely. Therefore, both the astronomical observations and the theoretical calculations support the reaction C + NH_3 being the main source of H_2NC in interstellar clouds.

Key words. astrochemistry – line: identification – molecular processes – ISM: molecules – radio lines: ISM

1. Introduction

The detection of H_2NC in the interstellar medium by Cabezas et al. (2021) came as a surprise. The observation of several groups of unidentified lines in the cold dense clouds L483 and B1-b motivated the search for potential carriers, among which H_2NC was not initially considered. Only after many plausible candidates were ruled out was H_2NC found to confidently reproduce the complex spectral pattern of astronomical lines. H_2NC was not initially considered as a plausible carrier because it is a high-energy isomer of H_2CN, which lies ∼30 kcal mol^{-1} above in energy (Puzzarini 2010; Cabezas et al. 2021). Moreover, there are two isomers not yet detected in space that are substantially more stable than H_2NC. These are the trans and cis forms of HCNH, which lie ∼8 and ∼13 kcal mol^{-1}, respectively, above the most stable isomer, H_2CN (Puzzarini 2010; Cabezas et al. 2021). It is worth noting that although H_2NC is the least stable member of this family of four isomers, it shows the most intense lines in L483 and B1-b.

The discovery of interstellar H_2NC came with several interesting implications. In addition to L483 and B1-b, H_2NC was also detected toward the $z = 0.89$ galaxy in front of the quasar PKS 1830−211, which is a high-redshift source exceptionally rich in molecules (Muller et al. 2011; Tercero et al. 2020). The fact that the abundance ratio H_2NC/H_2CN is ∼1 in L483 and B1-b and 0.27 toward PKS 1830−211 suggests that this ratio behaves like the HNC/HCN ratio, with values close to one in cold dense clouds and below one in diffuse clouds (Hirota et al. 1998; Sarrasin et al. 2010; Liszt & Lucas 2001). Surprisingly, neither H_2NC nor H_2CN were detected toward the cyanopolyyne peak of TMC-1 (hereafter TMC-1 CP) despite a previous claim of H_2CN detection in this cloud by Ohishi et al. (1994). While TMC-1 CP is a young starless core rich in carbon chains, L483 and B1-b are more evolved sources rich in molecules such as ammonia. The detection of H_2NC in L483 and B1-b and its non-detection in TMC-1 CP suggests that this species is more favored in NH_3-rich sources. This would be in line with the suspected chemical origin of H_2NC due to the reaction C + NH_3 (see the discussion in Cabezas et al. 2021).

In order to shed light on the issues raised by the discovery of H_2NC – that is, whether or not the H_2NC/H_2CN ratio behaves differently in dense and diffuse clouds, as occurs for the HNC/HCN ratio, and whether or not there is a correlation between the abundances of H_2NC and NH_3, which would reflect a chemical link between the two species – we carried out an observational survey to search for H_2NC, and simultaneously for H_2CN, toward a sample of dense and diffuse clouds with the 30 m telescope of the Institut de RadioAstronomie Millimétrique (IRAM). Here we report the results of this survey. We also present a computational study of the reaction between C and NH_3 aimed at investigating whether or not H_2NC can be

⋆ Based on observations carried out with the IRAM 30 m telescope. IRAM is supported by INSU/CNRS (France), MPG (Germany), and IGN (Spain).

Table 1. Source coordinates.

Source	RA(J2000.0)	Dec(J2000.0)
L1544	05:04:18.10	+25:10:48.0
L134N	15:54:06.55	−02:52:19.1
TMC-2	04:32:44.74	+24:24:33.5
Lupus-1A	15:42:52.40	−34:07:53.5
L1489	04:04:50.60	+26:18:29.4
TMC-1 NH3	04:41:23.02	+25:48:13.3
L1498	04:10:51.46	+25:09:58.2
L1641N	05:36:19.01	−06:22:13.3
B0415+379	04:18:21.28	+38:01:35.8
B0355+508	03:59:29.75	+50:57:50.2

formed in this reaction at the low temperatures of cold interstellar clouds.

2. Astronomical observations

The astronomical observations were carried out with the IRAM 30 m telescope in December 2021, April 2022, and June 2022. The weather conditions ranged from very good to moderate, with levels of precipitable water vapor in the range 1–10 mm. We used the EMIR (Eight MIxer Receiver) E090 receiver connected to a fast Fourier transform spectrometer that provides a spectral resolution of 48.8 kHz. We targeted the $1_{0,1}$–$0_{0,0}$ rotational transition of ortho H_2NC, which consists of multiple hyperfine components around 72.2 GHz, and the $1_{0,1}$–$0_{0,0}$ transition of ortho H_2CN, which has the strongest hyperfine components around 73.3 GHz. For both H_2NC and H_2CN, ortho levels have K_a even, while para levels have K_a odd.

We searched for H_2NC toward the cold dense clouds L1544, L134N, TMC-2, Lupus-1A, L1489, TMC-1 at the peak position of NH_3 (hereafter TMC-1 NH_3), L1498, and L1641N, and toward the diffuse clouds B0355+508 and B0415+379. The source coordinates are given in Table 1. The criteria to select these sources were bright emission of HNC, based on the expected analogy of the H_2NC/H_2CN and HNC/HCN ratios, and bright emission of NH_3, because of the potential correlation between H_2NC and NH_3. We used the studies of cold dense clouds by Suzuki et al. (1992) for ammonia data and by Hirota et al. (1998) for HNC data. We also included the dense core Lupus-1A because of its similarity to TMC-1 CP (Sakai et al. 2010). Regarding diffuse clouds, we included the two clouds from the Liszt & Lucas (2001) sample with the deepest absorption of HNC, B0415+379 and B0355+508, both of which also show deep absorption by NH_3 (Liszt et al. 2006).

For the cold dense clouds, the observations were carried out in the frequency-switching observing mode with a frequency throw of 7.2 MHz, while for the diffuse clouds we used the wobbler-switching observing mode with the secondary mirror nutating by 3′ at a rate of 0.5 Hz. Focus was checked at the beginning of each observing session and after sunrise and sunset, and pointing was regularly checked every 1 h. The intensity scale is expressed in terms of the antenna temperature corrected for atmospheric absorption and for antenna ohmic and spillover losses, T_A^*. The uncertainty in T_A^* is estimated to be around 10%. All data were reduced using the program CLASS from the software GILDAS[1].

[1] https://www.iram.fr/IRAMFR/GILDAS/

3. Astronomical results

3.1. Detections and non-detections of H_2NC and H_2CN

The high-energy isomer H_2NC turned out to be easier to detect than its more stable isomer H_2CN. We detected H_2NC in seven out of the eight cold dense clouds targeted (L1544, L134N, TMC-2, Lupus-1A, L1489, TMC-1 NH_3, and L1498; that is, in all but L1641N), while H_2CN was only detected in five of these sources (L1544, L134N, TMC-2, Lupus-1A, and L1489). Neither H_2NC nor H_2CN were detected in the two diffuse clouds observed, B0415+379 and B0355+508.

We searched for H_2NC through the $1_{0,1}$–$0_{0,0}$ transition, which lies around 72.2 GHz and spreads over ∼ 50 MHz due to fine and hyperfine splitting (see Cabezas et al. 2021). In Fig. 1 we show the part of the spectrum that covers the two brightest hyperfine components for the seven cold dense clouds where H_2NC was detected. The strongest component at 72194.211 MHz is well detected in the seven sources, while the second strongest one at 72 210.940 MHz is seen clearly in all sources except TMC-2, where it is only marginally detected. In addition, there are various weaker hyperfine components for which there is a good match between observed and calculated spectra. The line parameters for the two strongest components of H_2NC $1_{0,1}$–$0_{0,0}$ are given in Table 2. In the case of H_2CN, we targeted the $1_{0,1}$–$0_{0,0}$ transition, which lies around 73.3 GHz and also has a complex hyperfine pattern with components spread over almost 200 MHz. We show the observed spectra around the most intense component, lying at 73 349.648 MHz, for the five cold dense clouds where H_2CN was detected in Fig. 2. In some of the sources the weaker component at 73 345.486 MHz is also clearly seen. The line parameters for these two components are given in Table 2.

The two isomers H_2NC and H_2CN were also searched for toward the diffuse clouds B0415+379 and B0355+508, although neither were detected in these two sources. In Fig. 3, we show the observed spectra around the strongest hyperfine component of H_2NC and H_2CN, at 72 194.211 MHz and 73 349.648 MHz, respectively, for the two clouds. In addition, we show the observed spectra around the $1_{0,1}$–$0_{0,0}$ transition of H_2CO, lying at 72 837.949 MHz, which shows absorption at different velocities, in agreement with previous observations of other transitions of H_2CO toward these two sources (Liszt & Lucas 1995). The ordinate scale is expressed as line/continuum, following the convention by Liszt et al. (2006), where by 'line' we mean the T_A^* of the observed spectrum after baseline (or continuum) subtraction and by 'continuum' we mean the T_A^* of the continuum level. We find that the deepest H_2CO absorption in B0415+379 occurs at $V_{LSR} = -0.9$ km s^{-1}, while in B0355+508 it is located at a velocity of $V_{LSR} = -10.4$ km s^{-1}, in agreement with previous observations of simple molecules toward these two sources (e.g., Liszt & Lucas 1995, 2001; Liszt et al. 2006). As shown in Fig. 3, there is no hint of absorption by H_2NC or H_2CN toward either B0415+379 or B0355+508.

3.2. Calculation of column densities

We calculated column densities for H_2NC and H_2CN in sources where the molecule was detected. When the molecule was not detected, we computed an upper limit to the column density.

For the cold dense clouds L1544, L134N, TMC-2, Lupus-1A, L1489, TMC-1 NH_3, L1498, and L1641N we computed H_2NC and H_2CN column densities assuming local thermodynamic equilibrium. Since the observed hyperfine components of

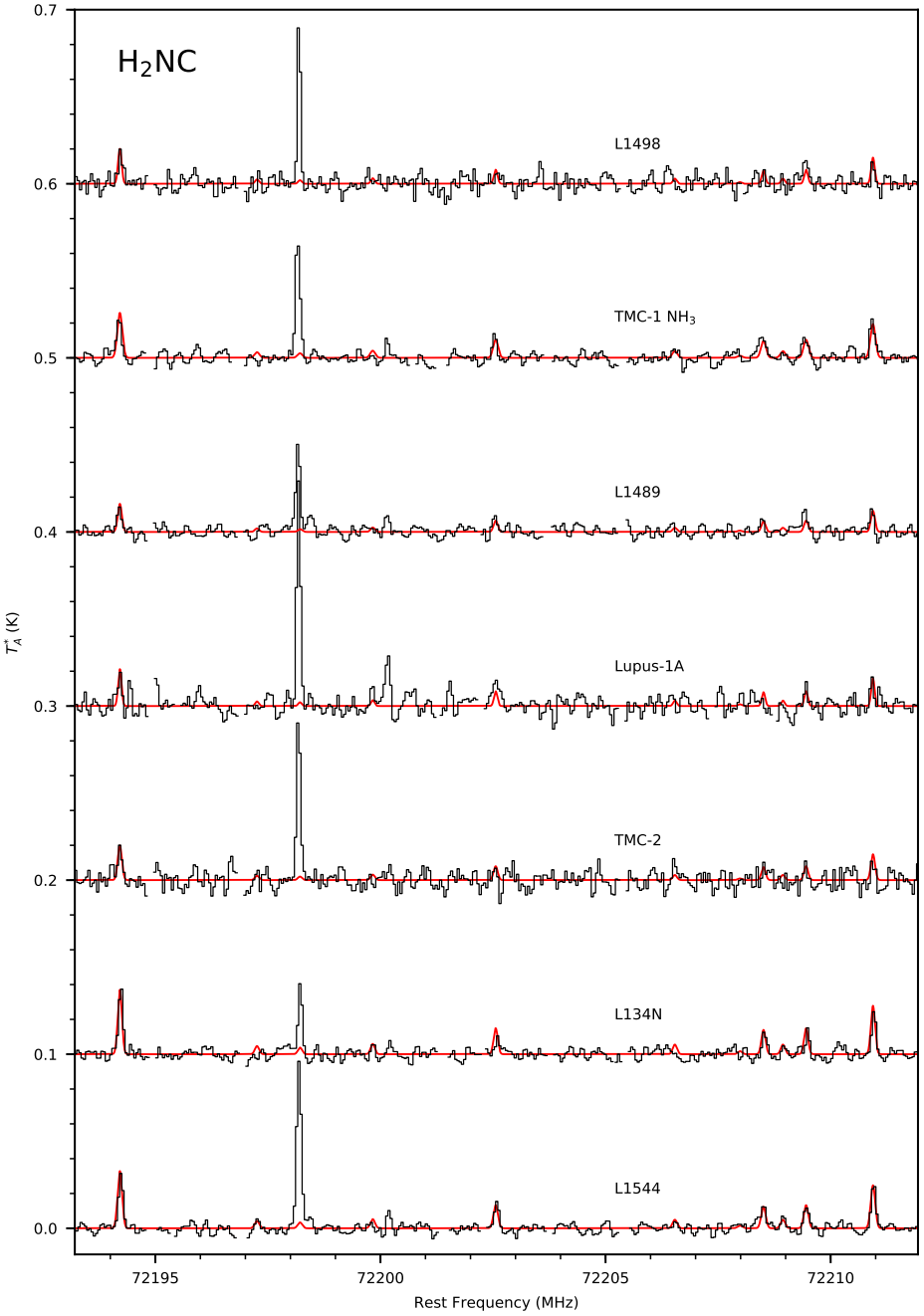

Fig. 1. Spectra of L1544, L134N, TMC-2, Lupus-1A, L1489, TMC-1 NH_3, and L1498 in the region covering the two most intense hyperfine components of the $1_{0,1}$–$0_{0,0}$ transition of H_2NC, at 72194.211 MHz and 72 210.940 MHz. In red we show the calculated synthetic spectra for H_2NC, adopting the column densities given in Table 3, an ortho-to-para ratio of 3, a rotational temperature of 4.0 K, a line width consistent with the values derived from the observations (see Table 2), and an emission size that fills the IRAM 30 m main beam. The bright line around 72 198 MHz corresponds to C_2D (see Cabezas et al. 2021).

H_2NC and H_2CN belong to the same rotational transition, the $1_{0,1}$–$0_{0,0}$ for both molecules, the detected lines have very similar upper level energies and thus it is not possible to determine the rotational temperature. For L483, Cabezas et al. (2021) derive a rotational temperature of 4.0 K for both H_2NC and H_2CN from the observation of various rotational transitions with different upper level energies. This value is lower than the gas kinetic temperature (around 10 K in L483; Anglada et al. 1997; Agúndez et al. 2019), which indicates sub-thermal excitation, in line with the fact that these two molecules have high dipole moments (3.83 D for H_2NC and 2.54 D for H_2CN; Cabezas et al. 2021; Cowles et al. 1991). Since cold dense clouds typically have kinetic temperatures around 10 K and H_2 volume densities of a few times 10^4 cm^{-3} (Benson & Myers 1989), in the absence of better constraints we adopted the rotational temperature derived in L483 for both H_2NC and H_2CN, 4.0 K, for all the cold dense clouds. We however note that the excitation of H_2NC and H_2CN could be different, as found for other isomers such as HCN and HNC (Hernández Vera et al. 2017) or the family of isomers of cyanoacetylene (Bop et al. 2019). In the case of H_2NC and H_2CN, collision rate coefficients are not available and thus we cannot investigate this point, although we acknowledge that this introduces an uncertainty in the calculation of the column densities. Cabezas et al. (2021) also show that the ortho-to-para ratio of H_2NC in L483 is consistent with the statistical value of three. We adopted this value for both H_2NC and H_2CN, although we note that this is an additional source of uncertainty in the calculation of the column densities. With these assumptions, we computed synthetic spectra for H_2NC and H_2CN adopting as line width a value consistent with that observed in each source (see Table 2). The synthetic spectra calculated for H_2NC and H_2CN are compared with the observed ones in Figs. 1 and 2,

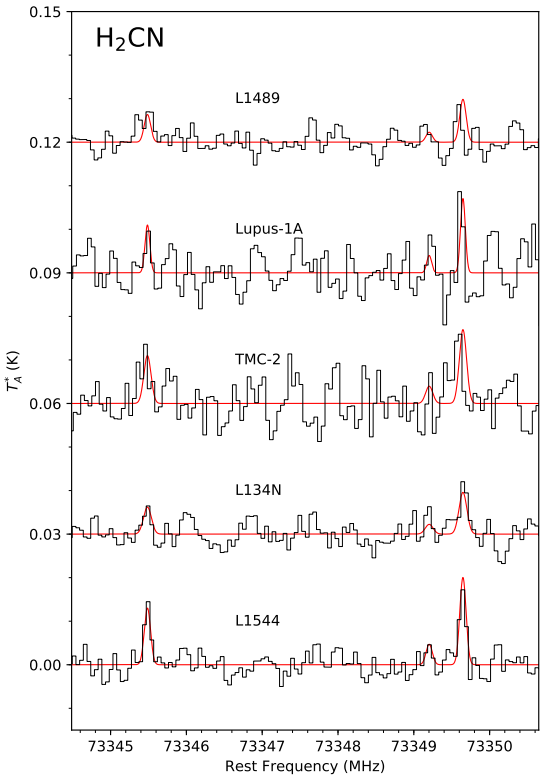

Fig. 2. Spectra of L1544, L134N, TMC-2, Lupus-1A, and L1489 in the region covering two of the brightest hyperfine components of the $1_{0,1}$–$0_{0,0}$ transition of H_2CN, lying at 73 345.486 MHz and 73 349.648 MHz. In red we superimpose the computed synthetic spectra for H_2CN, adopting the column densities given in Table 3, an ortho-to-para ratio of 3, a rotational temperature of 4.0 K, a line width consistent with the values derived from the observations (see Table 2), and an emission size that fills the IRAM 30 m main beam.

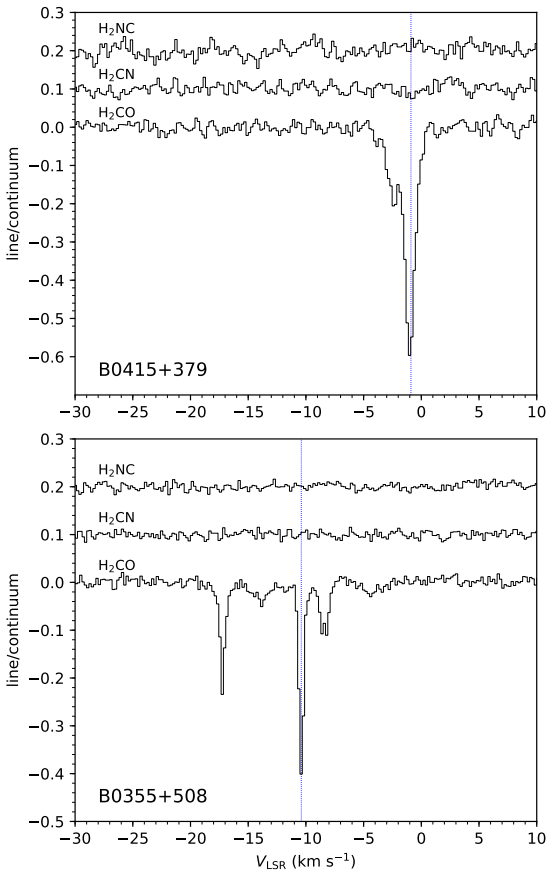

Fig. 3. Spectra of B0415+379 and B0355+508 at the frequencies of H_2CO $1_{0,1}$–$0_{0,0}$ (72 837.949 MHz) and of the strongest hyperfine component of H_2NC and H_2CN (72 194.211 MHz and 73 349.648 MHz, respectively). The y-axis is expressed as line/continuum. The position of the deepest absorption of H_2CO, $V_{LSR} = -0.9$ km s^{-1} in B0415+379 and $V_{LSR} = -10.4$ km s^{-1} in B0355+508, is indicated by a vertical dotted blue line.

respectively, while the corresponding derived column densities are given in Table 3.

In the case of non-detections of either H_2NC or H_2CN in cold dense clouds, we derived 3 σ upper limits to the column density, which are also given in Table 3. The only reported detection of H_2NC or H_2CN in the sources observed here is that of H_2CN in L1544 by Vastel et al. (2019). The column density derived here, 3.9×10^{11} cm^{-2} (see Table 3), is in agreement with the range of values found by Vastel et al. (2019), (3–6) $\times 10^{11}$ cm^{-2}.

In the case of the diffuse clouds B0415+379 and B0355+508, we derived upper limits to the column densities of H_2NC and H_2CN in the following way. We first computed the line opacity, τ, using the equation (e.g., Linke et al. 1981; Nyman 1984; Greaves et al. 1992; Corby et al. 2018)

$$\tau = -\mathrm{Ln}\left(1 + \frac{\mathrm{line}}{\mathrm{continuum}}\right). \quad (1)$$

The velocity-integrated opacity, $\int \tau \mathrm{d}v$, is then related to the column density, N, through the expression (Nyman 1984; Greaves & Nyman 1996; Corby et al. 2018)

$$\int \tau \mathrm{d}v = \frac{N}{Q(T_{\mathrm{rot}})} \frac{8\pi^3 S \mu^2}{3h} \left(\mathrm{e}^{-E_{\mathrm{l}}/kT_{\mathrm{rot}}} - \mathrm{e}^{-E_{\mathrm{u}}/kT_{\mathrm{rot}}}\right), \quad (2)$$

where T_{rot} is the rotational temperature, $Q(T_{\mathrm{rot}})$ is the partition function, S is the line strength, μ is the dipole moment, E_{l} and E_{u} are the energies of the lower and upper level, respectively, and h and k are the Planck and Boltzmann constants, respectively. For convenience, Eq. (2) can be expressed as

$$\int \tau \mathrm{d}v = \frac{N}{Q(T_{\mathrm{rot}})} \frac{S\mu^2}{8.0 \times 10^{12}} \left(\mathrm{e}^{-E_{\mathrm{l}}/T_{\mathrm{rot}}} - \mathrm{e}^{-E_{\mathrm{u}}/T_{\mathrm{rot}}}\right), \quad (3)$$

where $\int \tau \mathrm{d}v$ is in units of km s^{-1}, N in cm^{-2}, μ in Debye, and E_{l}, E_{u}, and T_{rot} in K. We assumed a rotational temperature equal to that of the cosmic microwave background (i.e., 2.725 K). To derive upper limits to the column densities of H_2NC and H_2CN, we used the line parameters of the strongest hyperfine component, lying at 72 194.211 MHz and 73 349.648 MHz, respectively. For H_2NC, $\mu = 3.83$ D, $Q(2.725\,\mathrm{K}) = 35.075$, $S = 2.67$, $E_{\mathrm{l}} = 0.012$ K, and $E_{\mathrm{u}} = 3.477$ K, while for H_2CN, $\mu = 2.54$ D, $Q(2.725\,\mathrm{K}) = 34.597$, $S = 2.67$, $E_{\mathrm{l}} = 0.018$ K, and $E_{\mathrm{u}} = 3.538$ K. The 3 σ upper limits to the column densities of H_2NC and H_2CN in B0415+379 and B0355+508 are given in Table 3. As a reference, the column densities derived for para-H_2CO are 4.0×10^{12} cm^{-2} in B0415+379 at $V_{LSR} = -0.9$ km s^{-1} and 1.1×10^{12} cm^{-2} in B0355+508 at $V_{LSR} = -10.4$ km s^{-1}, values that are very similar to those derived by Liszt & Lucas (1995).

4. Astrophysical lessons on H_2NC and H_2CN

The column densities derived for H_2NC and H_2CN are typically in the range 10^{11}–10^{12} cm^{-2}; the largest values are found

Table 2. Line parameters of the strongest hyperfine components of H_2NC and H_2CN.

Source	Molecule	Transition	ν_{calc} (MHz)	V_{LSR} (km s^{-1})	Δv (km s^{-1})	T_A^* peak (mK)	$\int T_A^* dv$ (mK km s^{-1})
L1544	H_2NC	$1_{0,1}$–$0_{0,0}$ $J = 1.5$–0.5 $F_1 = 2.5$–1.5 $F = 3.5$–2.5	72 194.211	7.10(2)	0.49(4)	31.7(2)	16.5(10)
L1544	H_2NC	$1_{0,1}$–$0_{0,0}$ $J = 1.5$–0.5 $F_1 = 2.5$–1.5 $F = 2.5$–1.5	72 210.940	7.13(3)	0.48(6)	26.4(2)	13.4(14)
L134N	H_2NC	$1_{0,1}$–$0_{0,0}$ $J = 1.5$–0.5 $F_1 = 2.5$–1.5 $F = 3.5$–2.5	72 194.211	2.40(2)	0.47(3)	39.4(3)	19.6(10)
L134N	H_2NC	$1_{0,1}$–$0_{0,0}$ $J = 1.5$–0.5 $F_1 = 2.5$–1.5 $F = 2.5$–1.5	72 210.940	2.40(3)	0.43(6)	25.7(3)	11.8(15)
TMC-2	H_2NC	$1_{0,1}$–$0_{0,0}$ $J = 1.5$–0.5 $F_1 = 2.5$–1.5 $F = 3.5$–2.5	72 194.211	6.19(5)	0.45(13)	19.4(5)	9.3(21)
TMC-2	H_2NC	$1_{0,1}$–$0_{0,0}$ $J = 1.5$–0.5 $F_1 = 2.5$–1.5 $F = 2.5$–1.5	72 210.940	6.25(4)	0.20(10)	16.8(5)	3.6(16) [a]
Lupus-1A	H_2NC	$1_{0,1}$–$0_{0,0}$ $J = 1.5$–0.5 $F_1 = 2.5$–1.5 $F = 3.5$–2.5	72 194.211	5.00(8)	0.40(19)	18.9(5)	8.0(27)
Lupus-1A	H_2NC	$1_{0,1}$–$0_{0,0}$ $J = 1.5$–0.5 $F_1 = 2.5$–1.5 $F = 2.5$–1.5	72 210.940	5.11(5)	0.34(10)	17.7(5)	6.4(17)
L1489	H_2NC	$1_{0,1}$–$0_{0,0}$ $J = 1.5$–0.5 $F_1 = 2.5$–1.5 $F = 3.5$–2.5	72 194.211	6.66(4)	0.50(9)	14.1(3)	7.4(12)
L1489	H_2NC	$1_{0,1}$–$0_{0,0}$ $J = 1.5$–0.5 $F_1 = 2.5$–1.5 $F = 2.5$–1.5	72 210.940	6.71(5)	0.39(10)	14.2(3)	5.9(14)
TMC-1 NH_3	H_2NC	$1_{0,1}$–$0_{0,0}$ $J = 1.5$–0.5 $F_1 = 2.5$–1.5 $F = 3.5$–2.5	72 194.211	5.89(3)	0.54(8)	22.8(2)	13.0(17)
TMC-1 NH_3	H_2NC	$1_{0,1}$–$0_{0,0}$ $J = 1.5$–0.5 $F_1 = 2.5$–1.5 $F = 2.5$–1.5	72 210.940	5.86(4)	0.54(9)	22.4(2)	12.7(18)
L1498	H_2NC	$1_{0,1}$–$0_{0,0}$ $J = 1.5$–0.5 $F_1 = 2.5$–1.5 $F = 3.5$–2.5	72 194.211	7.71(5)	0.57(14)	16.7(4)	10.2(20)
L1498	H_2NC	$1_{0,1}$–$0_{0,0}$ $J = 1.5$–0.5 $F_1 = 2.5$–1.5 $F = 2.5$–1.5	72 210.940	7.80(2)	0.20(10)	20.2(4)	4.4(13)
L1544	H_2CN	$1_{0,1}$–$0_{0,0}$ $J = 1.5$–0.5 $F_1 = 2.5$–1.5 $F = 2.5$–1.5	73 345.486	7.19(3)	0.39(7)	14.9(2)	6.2(9)
L1544	H_2CN	$1_{0,1}$–$0_{0,0}$ $J = 1.5$–0.5 $F_1 = 2.5$–1.5 $F = 3.5$–2.5	73 349.648	7.23(3)	0.40(5)	17.8(2)	7.6(9)
L134N	H_2CN	$1_{0,1}$–$0_{0,0}$ $J = 1.5$–0.5 $F_1 = 2.5$–1.5 $F = 2.5$–1.5	73 345.486	2.53(7)	0.40(15)	6.6(2)	2.8(9) [a]
L134N	H_2CN	$1_{0,1}$–$0_{0,0}$ $J = 1.5$–0.5 $F_1 = 2.5$–1.5 $F = 3.5$–2.5	73 349.648	2.45(5)	0.50(15)	11.8(2)	6.3(14)
TMC-2	H_2CN	$1_{0,1}$–$0_{0,0}$ $J = 1.5$–0.5 $F_1 = 2.5$–1.5 $F = 2.5$–1.5	73 345.486	6.40(11)	0.67(22)	10.5(4)	7.5(23)
TMC-2	H_2CN	$1_{0,1}$–$0_{0,0}$ $J = 1.5$–0.5 $F_1 = 2.5$–1.5 $F = 3.5$–2.5	73 349.648	6.47(7)	0.46(20)	17.0(4)	8.2(25)
Lupus-1A	H_2CN	$1_{0,1}$–$0_{0,0}$ $J = 1.5$–0.5 $F_1 = 2.5$–1.5 $F = 2.5$–1.5	73 345.486	4.97(9)	0.31(16)	9.9(4)	3.3(16) [a]
Lupus-1A	H_2CN	$1_{0,1}$–$0_{0,0}$ $J = 1.5$–0.5 $F_1 = 2.5$–1.5 $F = 3.5$–2.5	73 349.648	5.10(2)	0.20(10)	28.9(4)	6.1(16)
L1489	H_2CN	$1_{0,1}$–$0_{0,0}$ $J = 1.5$–0.5 $F_1 = 2.5$–1.5 $F = 2.5$–1.5	73 345.486	6.49(5)	0.49(13)	7.8(2)	4.1(9)
L1489	H_2CN	$1_{0,1}$–$0_{0,0}$ $J = 1.5$–0.5 $F_1 = 2.5$–1.5 $F = 3.5$–2.5	73 349.648	6.86(5)	0.33(8)	9.1(2)	3.2(8)

Notes. The line parameters V_{LSR}, Δv (full width at half maximum), T_A^* peak, and $\int T_A^* dv$ were derived from a Gaussian fit to the line profile. Numbers in parentheses are 1σ uncertainties in units of the last digits. [a]Marginal detection.

Table 3. Column densities of H_2NC and H_2CN.

Source	$N(H_2NC)$ (cm^{-2})	$N(H_2CN)$ (cm^{-2})	H_2NC/H_2CN	Reference	$N(NH_3)$ (cm^{-2})	Reference
Cold dense clouds						
L483	1.0×10^{12}	8.0×10^{11}	1.25	(1)	14×10^{14}	(3)
B1-b	1.0×10^{12}	1.0×10^{12}	1.00	(1)	11.2×10^{14}	(4)
TMC-1 CP	$<3.2 \times 10^{11}$	$<4.8 \times 10^{11}$	–	(1)	1.9×10^{14}	(4)
L1544	3.9×10^{11}	4.3×10^{11}	0.91	(2)	2.7×10^{14}	(4)
L134N	4.0×10^{11}	2.5×10^{11}	1.60	(2)	7.8×10^{14}	(4)
TMC-2	2.1×10^{11}	4.1×10^{11}	0.51	(2)	6.1×10^{14}	(4)
Lupus-1A	1.9×10^{11}	2.8×10^{11}	0.68	(2)	1.1×10^{14}	(5)
L1489	1.7×10^{11}	2.1×10^{11}	0.81	(2)	6.3×10^{14}	(4)
TMC-1 NH_3	3.3×10^{11}	$<1.2 \times 10^{11}$	>2.7	(2)	5.2×10^{14}	(4)
L1498	1.9×10^{11}	$<1.4 \times 10^{11}$	>1.4	(2)	4.1×10^{14}	(4)
L1641N	$<3.1 \times 10^{11}$	$<4.6 \times 10^{11}$	–	(2)	11.0×10^{14}	(4)
Diffuse-like clouds						
PKS 1830−211	5.3×10^{11}	2.0×10^{12}	0.27	(1)	$(5–10) \times 10^{14}$	(6)
B0415+379	$<3.1 \times 10^{11}$	$<5.5 \times 10^{11}$	–	(2)	10.53×10^{12}	(7)
B0355+508	$<9.2 \times 10^{10}$	$<2.0 \times 10^{11}$	–	(2)	2.54×10^{12}	(7)

References. (1) Cabezas et al. (2021), (2) this work, (3) Anglada et al. (1997), (4) Suzuki et al. (1992), (5) value at position Lup1 C4, ~2 arcmin off from Lupus-1A (Benedettini et al. 2012), (6) Henkel et al. (2008), (7) values at the velocity components $V_{LSR} = -0.9$ km s^{-1} for B0415+379 and $V_{LSR} = -10.4$ km s^{-1} for B0355+508 (Liszt et al. 2006).

for the cold dense clouds L483 and B1-b and the $z = 0.89$ galaxy in front of PKS 1830−211, which happen to be the three sources where H_2NC was initially discovered by Cabezas et al. (2021). On the other hand, the H_2NC/H_2CN abundance ratio is relatively uniform around unity, with the lowest value of 0.27 found toward PKS 1830−211 and the largest one, > 2.7, occurring in the cold dense cloud TMC-1 NH_3. We aim to understand whether the abundances of H_2NC and H_2CN, or the abundance ratio H_2NC/H_2CN, depend on some physical or chemical characteristic of the host cloud.

Cabezas et al. (2021) proposed that the H_2NC/H_2CN ratio could behave like the HNC/HCN ratio, with values close to one in cold dense clouds and below one in diffuse clouds. This idea was suggested by the fact that the H_2NC/H_2CN ratio derived in the cold dense clouds L483 and B1-b was ∼1, while in the redshifted galaxy in front of the quasar PKS 1830−211, which has a chemical composition characteristic of a diffuse or translucent cloud, the H_2NC/H_2CN ratio was found to be 0.27. With this idea in mind, in this study we searched for H_2NC and H_2CN in various cold dense clouds and in the two most promising diffuse clouds known to contain a relatively rich molecular content, based on the series of studies by Liszt and Lucas (e.g., Liszt & Lucas 2001; Liszt et al. 2006). The observations of cold dense clouds carried out here confirm that the H_2NC/H_2CN ratio is close to one in this type of source, with the largest deviation occurring for TMC-1 NH_3, where the detection of H_2NC and the non-detection of H_2CN set a lower limit to the H_2NC/H_2CN of 2.7. However, we did not detect H_2NC or H_2CN toward the diffuse clouds B0415+379 and B0355+508, making it impossible to constrain the H_2NC/H_2CN ratio in galactic diffuse clouds. The non-detection of H_2NC and H_2CN in these two diffuse clouds is probably related to the low column density of NH_3 compared to the typical column densities of NH_3 in cold dense clouds, which are one to two orders of magnitude higher (see the discussion on this point below). The sensitivity achieved in the IRAM 30 m observations of these two diffuse clouds, in particular for B0415+379, where the T_A^* rms noise level reached is ∼4 mK, suggests that it would be challenging to detect either H_2NC or H_2CN in a galactic diffuse cloud. It seems therefore difficult to confirm whether or not the H_2NC/H_2CN ratio is significantly lower in diffuse clouds than in cold dense clouds.

Another interesting feature discussed by Cabezas et al. (2021) concerns the chemical origin of H_2NC. The reactions N + CH_3 and C + NH_3 are two potentially important sources of H_2NC. Chemical routes to H_2NC involving ions are also possible. For example, the dissociative recombination of cations, such as CH_3N^+, $CH_2NH_2^+$, $CH_3NH_2^+$, or $CH_3NH_3^+$, with electrons could produce as fragments H_2NC and H_2CN, although experimental or theoretical information on these reactions is scarce (Yuen et al. 2019). A similar mechanism operates in cold dense clouds for HCN and HNC, with the two isomers being formed with nearly equal yields upon dissociative recombination of $HCNH^+$ with electrons (Mendes et al. 2012). The reaction C + NH_3 is a more likely source of H_2NC than N + CH_3 because it involves a smaller rearrangement of atoms. If the reaction C + NH_3 is the main pathway to H_2NC, we could expect a relation between the abundance of H_2NC and that of NH_3. To investigate this point we represent in Fig. 4 the column density of H_2NC versus that of NH_3. Some interesting features emerge from this plot. First, the two sources with the largest column densities of H_2NC, which are L483 and B1-b, also have the highest column densities of NH_3. Second, among the cold dense clouds, the sources with the lowest column densities of NH_3, Lupus-1A and TMC-1 CP, also have low column densities of H_2NC. These two findings are very suggestive of a relation between H_2NC and NH_3, and thus of NH_3 being a precursor of H_2NC. Cold dense clouds with intermediate NH_3 column densities, higher than those of Lupus-1A and TMC-1 CP but lower than those of L483 and B1-b, show a less clear relation between H_2NC and NH_3. In particular, there are sources, such as L1498, L1489, TMC-2, and L1641N, that have a moderately high column density of NH_3 but a low H_2NC column density. This fact suggests that NH_3 may not be the only species that regulates the abundance of H_2NC. Indeed, if H_2NC is mainly formed by the reaction C + NH_3, the abundance of atomic carbon would also be a relevant parameter setting the abundance of H_2NC. However, it is very difficult to constrain the abundance of atomic carbon inside cold dense clouds (Schilke et al. 1995; Stark et al. 1996). Diffuse clouds have a markedly different chemistry compared to cold dense clouds, with less chemical complexity (e.g., Liszt et al. 2008). This may be the reason why H_2NC and H_2CN were not detected toward B0415+379 or B0355+508. However, if the relation between H_2NC and NH_3 found for cold dense clouds holds down to the diffuse stage, the reason for the non-detection of H_2NC and H_2CN toward B0415+379 or B0355+508 could be the low NH_3 column density in these two sources, one to two orders of magnitude smaller than in cold dense clouds (see Fig. 4).

5. The reaction C + NH_3 as a source of H_2NC

The suspected chemical link between H_2NC and NH_3 in interstellar clouds may be attributed to the fact that the reaction C + NH_3 is the main formation mechanism of H_2NC in these environments. Here we revisit this reaction and investigate whether H_2NC can be produced this way.

5.1. Previous studies

The reaction C + NH_3 has been found to be fast at low temperatures, with a measured rate coefficient of $(1.8 \pm 0.2) \times 10^{-10}$ cm^3 s^{-1} at 50 K (Hickson et al. 2015). The reaction products,

$$C(^3P) + NH_3(^1A') \rightarrow H(^2S) + H_2CN(^2B_2) \quad (4a)$$
$$\rightarrow H(^2S) + \text{trans-HCNH}(^2A') \quad (4b)$$
$$\rightarrow H(^2S) + \text{cis-HCNH}(^2A') \quad (4c)$$
$$\rightarrow H(^2S) + H_2NC(^2B_2), \quad (4d)$$

were investigated by Bourgalais et al. (2015). These authors measured the H atom yield to be 0.99 ± 0.08, independent of temperature, over the 50–296 K range. On the other hand, they also used tunable vacuum-ultraviolet photoionization coupled with time-of-flight mass spectrometry in a gas flow tube experiment at 330 K, which indicated that H_2CN, and not cis or trans HCNH, is likely the main isomer produced. Bourgalais et al. (2015) also performed electronic structure calculations, which indicated that the reactants approach each other in an attractive potential, which leads to the formation of the intermediate CNH_3 (hereafter I_4; see Fig. 5). From I_4 the dynamics can proceed by over-passing two barriers. The lower is TS_{I3I4}, which connects I_4 to I_3 and gives access to the statistical reaction mechanism that is expected to majoritarily lead to H_2CN. The second barrier, TS_{I4P4}, connects I_4 directly with the H_2NC product and, according to Bourgalais et al. (2015), has an energy slightly above that of the reactants (although this is very method dependent), which implies that this pathway is closed at a temperature of 10 K. As a

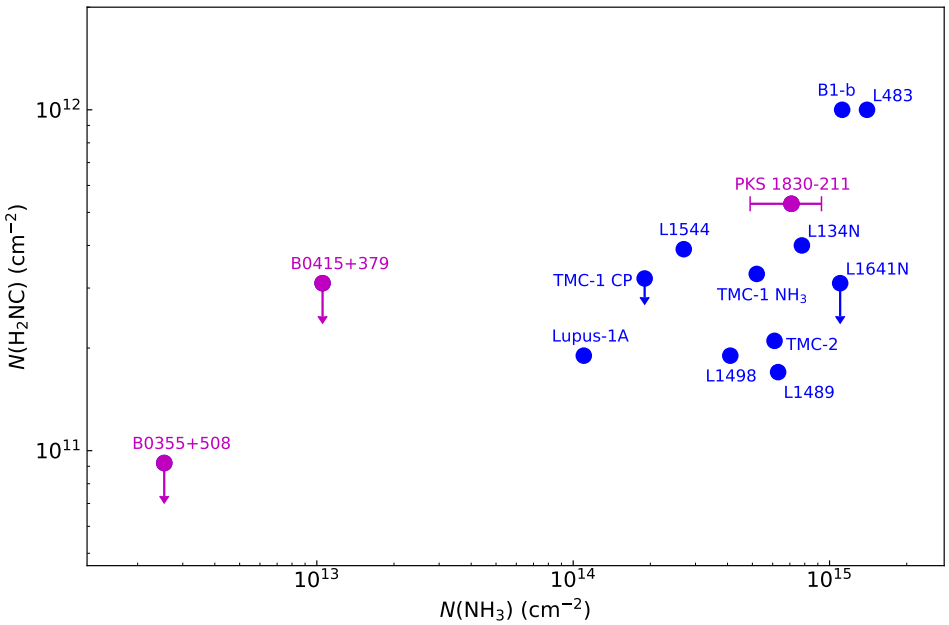

Fig. 4. Column density of H_2NC represented as a function of the column density of NH_3 for the sources where H_2NC has been searched for. Cold dense clouds are plotted in blue and diffuse-like clouds in magenta. The values of the column densities and the corresponding references are given in Table 3.

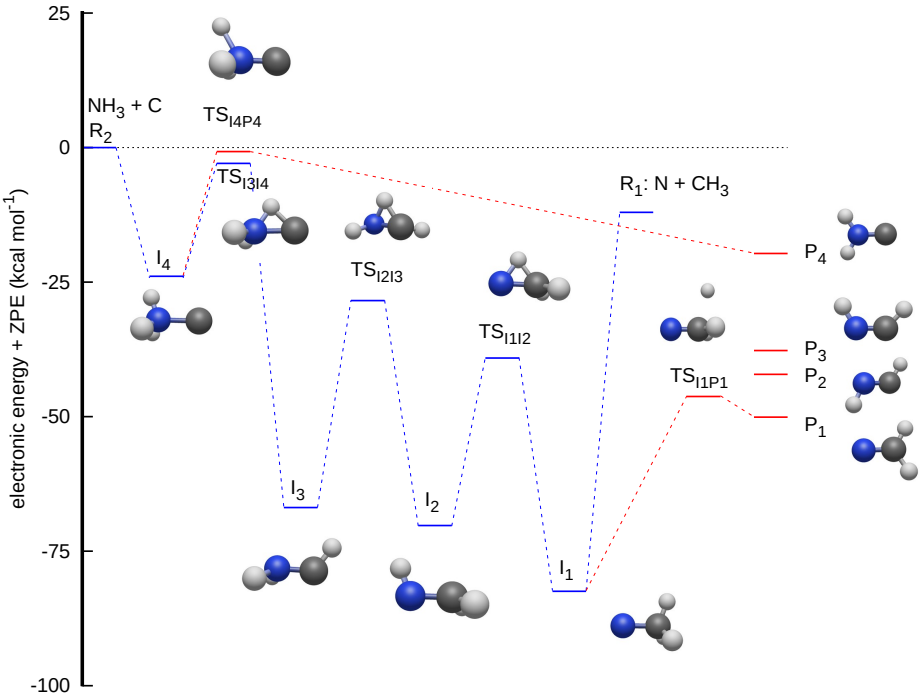

Fig. 5. Energies (in kcal mol^{-1}) of the stationary points describing the C + NH_3 reaction in the triplet state obtained at RCCSD(T)-F12 with the VQZ-F12 basis set, including the ZPE. All energies are relative to the $C(^3P)$ + $NH_3(^1A')$ reactants.

consequence, Bourgalais et al. (2015) assigned a branching ratio of 100% to channel (4a).

It is also interesting to discuss the reaction N + CH_3 because it occurs on the same triplet potential energy surface (PES) as C + NH_3. This reaction has been studied experimentally (Stief et al. 1988; Marston et al. 1989a,b) and theoretically (González & Schlegel 1992; Sadygov & Yarkony 1997; Cimas & Largo 2006; Alves et al. 2008; Chiba et al. 2015). The rate coefficient has been measured to be $(0.64–1.7) \times 10^{-10}$ cm^3 s^{-1} in the temperature range 200–423 K (Marston et al. 1989a). The major reaction products have been experimentally inferred to be H_2CN + H, with about 10% of the reaction leading to HCN + H_2 (Marston et al. 1989b). This has been theoretically explained in terms of an intersystem crossing from the triplet to the singlet PES (González & Schlegel 1992; Sadygov & Yarkony 1997; Chiba et al. 2015). The mechanism of the reaction has been discussed in detail by Cimas & Largo (2006). The reactants approach each other in an attractive potential to form the intermediate NCH_3 (hereafter I_1; see Fig. 5), which is connected to two saddle points: the lower is TS_{I1P1}, which yields H_2CN as a product, while the higher, TS_{I1I2}, connects to the $HCNH_2$ intermediate (I_2). The two barriers are submerged (i.e., have energies below that of

Table 4. Electronic energies, E_{el}, calculated at the RCCSD(T)-F12/VQZ-F12 level, zero-point energies (ZPEs), and the sum of both for the stationary points involved in the C + NH_3 reaction in the triplet state.

Name	System	E_{el}	ZPE	E_{el} + ZPE
R_2	$C(^3P)+NH_3(^1A')$	0.0	21.599	0.0
R_1	$N(^4S)+CH_3(^2A_2'')$	−9.153	18.718	−12.033
I_4	C-NH_3	−26.884	24.580	−23.902
I_3	HC-NH_2	−68.771	23.487	−66.882
I_2	H_2C-NH	−71.036	22.392	−70.235
I_1	H_3C-N	−84.210	23.353	−82.455
P_4	H + H_2NC	−14.745	16.664	−19.680
P_3	H + cis-HCNH	−31.780	15.651	−37.727
P_2	H + trans-HCNH	−36.775	16.244	−42.129
P_1	H + H_2CN	−44.274	15.780	−50.092
TS_{I3I4}	$CHNH_2$	−1.750	20.420	−2.929
TS_{I2I3}	HCHNH	−26.836	20.007	−28.427
TS_{I1I2}	H_2CHN	−37.337	19.825	−39.111
TS_{I4P4}	CNH_2-H	1.547	19.306	−0.745
TS_{I1P1}	H-H_2CN	−41.726	17.062	−46.262

Notes. Energies are relative to C + NH_3 (R_2). All values are in units of kcal mol^{-1}. The calculation of E_{el} for N + CH_3 (R_1) was done independently for each subsystem, and their energies were added. The imaginary frequencies at the saddle points TS_{I3I4}, TS_{I2I3}, TS_{I1I2}, TS_{I4P4}, and TS_{I1P1} are 4.837, 5.719, 5.578, 5.154, and 2.283 kcal mol^{-1}, respectively.

the reactants N + CH_3); however, since TS_{I1P1} < TS_{I1I2}, according to Rice–Ramsperger–Kassel–Marcus (RRKM) theory, most of the flux will go through TS_{I1P1} to form H_2CN. The I_2 intermediate in turn is connected to I_3 (H_2NCH). The path along these intermediates, $I_1 \rightarrow I_2 \rightarrow I_3$, in which successive H atom migrations take place, is expected to behave statistically, and therefore the main product along this second statistical reaction mechanism is also expected to be H_2CN. Thus, Cimas & Largo (2006) conclude that the main products should be H + H_2CN.

5.2. Stationary points of the triplet electronic state

We carried out a progressive optimization of the stationary points of the triplet PES using several methods, M06-2X, RCCSD(T), and RCCSD(T)-F12, and different basis sets, VTZ-F12 and VQZ-F12 (Peterson & Werner 2008), using the MOLPRO package (Werner et al. 2012). The relative energies of the stationary points varied considerably depending on the method and basis set, especially for the transition states. This indicates that electronic correlation is very important. For every transition state, we calculated the intrinsic reaction coordinate to probe the two minima connected to it.

The RCCSD(T)-F12/VQZ-F12 results are listed in Table 4 and represented in Fig. 5. The height of TS_{I4P4} is critical since it connects the CNH_3 well, I_4, with the H_2NC product, P_4. The electronic energy of TS_{I4P4} determined via the RCCSD(T)-F12/VQZ-F12 method is above that of the reactants C + NH_3. However, when the zero-point energy (ZPE) is included, the energy at the TS_{I4P4} point becomes negative, and therefore the H_2NC product becomes accessible in the C + NH_3 reaction even at low temperatures.

The computational effort of geometry optimization increases dramatically with the size of the basis set, especially when the gradients and Hessians need to be calculated numerically, as happens when using RCCSD(T)-F12 methods. An alternative is to extrapolate the energies obtained with two or more electronic correlation-consistent basis sets to the complete basis set (CBS) limit. There are many extrapolation methods, and some of them were reviewed and applied to H_3^+ by Velilla et al. (2010), who found that the best option is the two-point extrapolation method (Lee & Park 2000; Huh & Lee 2003):

$$E_X = E_{CBS} + A(X + k)^{-3}, \quad (5)$$

where X refers to the basis ($X = 3$ and 4 for VTZ and VQZ, respectively) and $k = -1$ is the best choice when using RCCSD(T) methods. The results are listed in Table 5. In the CBS limit, the transition states TS_{I4P4} and TS_{I3I4} have similar energies, both lying below that of the reactants C + NH_3, as found with the RCCSD(T)-F12/VQZ-F12 method.

Table 5. Electronic energies calculated at the complete basis set (CBS) limit, E_{CBS}, using the RCCSD(T)-F12, MRCI-F12, and MRCI-F12+Q methods plus the ZPE.

Name	E_{CBS} + ZPE		
	RCCSD(T)-F12	MRCI-F12	MRCI-F12+Q
R_2	0.0	0.0	0.0
I_4	−25.395	−29.574	−28.455
TS_{I3I4}	−3.907	−7.567	−7.392
TS_{I4P4}	−1.568	−7.260	−6.266

Notes. Energies are relative to C + NH_3 (R_2). All values are in units of kcal mol^{-1}. CBS energies obtained using Eq. (5) with the VTZ-F12 and VQZ-F12 basis sets, where in both cases electronic energies are obtained at the geometries optimized using RCCSD(T)-F12/VQZ-F12.

Single reference methods such as RCCSD(T)-F12 have problems describing reactions, especially at the saddle points, which usually have a strong large multi-reference character. In the RCCSD(T)-F12 calculations discussed above, the T1 diagnostic is always below 0.023, as previously found by Bourgalais et al. (2015). This value indicates that RCCSD(T)-F12 results can be considered reasonably good even at saddle points (Lee & Taylor 1989). Multi-reference methods, such as the multi-reference configuration interaction (MRCI) method (Werner & Knowles 1988; Shiozaki & Werner 2013), are considered more accurate for describing reactions, especially at saddle points. Since MRCI calculations are more computationally demanding, here we performed single-point calculations at the geometries optimized with the RCCSD(T)-F12/VQZ-F12 method, with and without the Davidson correction (Davidson 1975), which we denote as MRCI-F12 and MRCI-F12+Q, respectively. The results obtained with the VTZ and VQZ basis sets were then used to obtain the complete basis limit, which is listed in Table 5. The heights of the reaction barriers TS_{I3I4} and TS_{I4P4} as determined via the MRCI-F12 and MRCI-F12+Q methods are lower than with the RCCSD(T)-F12 method, and, interestingly, the energies of these two transition states become much more similar to each other.

5.3. Reaction rate coefficient and RRKM branching ratios

At low energies, the two reactants approach each other, forming the CNH_3 intermediate I_4, following a descendent potential energy path with no barrier. This is a clear example of a capture mechanism, which is governed by long-range interactions at low temperatures. Long-range forces are due to the interaction of the

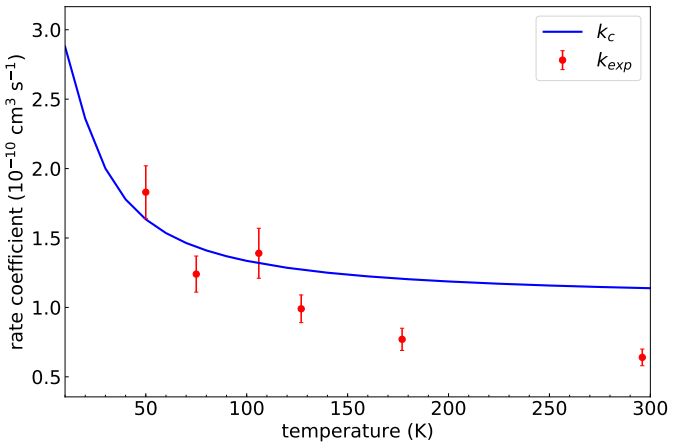

Fig. 6. Capture rate coefficient, k_c, calculated for the reaction C + NH_3 according to Eq. (7) compared with the experimental measurements of the reactive rate coefficient by Hickson et al. (2015).

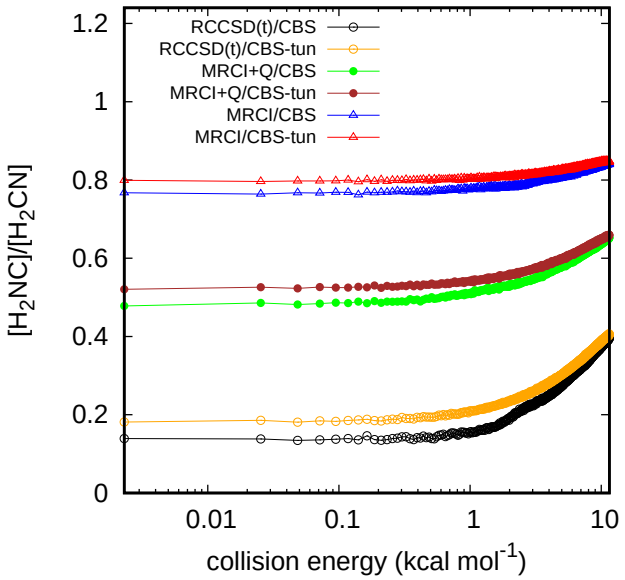

Fig. 7. Product branching ratio [H_2NC]/[H_2CN] obtained for the reaction C + NH_3 using the VQZ-F12 and CBS results according to Eq. (9), with and without tunneling.

electric dipole and quadrupole of NH_3 with the quadrupole of the p state of C(^{3}P). The long-range potential, V_{LR}, varies as a function of R (the distance between the C atom and the center of mass of NH_3) as (Zeimen et al. 2003)

$$V_{LR}(R,\theta) = M_{QD}(\theta)\frac{Q(\mathrm{C})D(\mathrm{NH_3})}{R^4} + M_{QQ}(\theta)\frac{Q(\mathrm{C})Q(\mathrm{NH_3})}{R^5}, \quad (6)$$

where Q(C) and Q(NH_3) are the quadrupoles of C and NH_3, respectively, D(NH_3) is the dipole moment of NH_3, and $M_{QD}(\theta)$ and $M_{QQ}(\theta)$ are 3×3 matrices that account for the quadrupole–dipole and quadrupole–quadrupole interactions, respectively (Zeimen et al. 2003). In the present treatment we neglect the quadrupole–quadrupole contribution and the dependence on the angle θ. We thus considered an isotropic long-range potential A/R^4, where $A = 2\,M_{QD}\,Q(\mathrm{C})\,D(\mathrm{NH_3})$. The parameter A is obtained via fitting to CCSD(T) calculations, with the aVTZ basis set. The ab initio calculations were done for NH_3 in its equilibrium geometry, with its symmetry axis along the z-axis and its center of mass at origin, and the $R = z$ coordinate of the C atom varied. We obtain a value of $A = -0.85$ hartree bohr^4. Similar to the Langevin case, the capture rate coefficient, k_c, is then given by

$$k_c(T) = 2\pi\sqrt{A/\mu}\;\; q_e(T) = 3.13\times10^{-10}\,\mathrm{cm^3\,s^{-1}}\;\; q_e(T), \quad (7)$$

where μ is the reduced mass of the C + NH_3 system and q_e is the electronic partition function of C(^{3}P). Assuming that only the three lowest spin-orbit states of C(^{3}P) yield trapping, we get

$$q_e(T) = \frac{1 + 2\exp(-23.62/T)}{1 + 3\exp(-23.62/T) + 5\exp(-62.46/T)}. \quad (8)$$

The calculated capture rate coefficient is compared in Fig. 6 with the experimental reactive rate coefficient measured at different temperatures by Hickson et al. (2015). We note that the capture rate coefficient is an upper limit to the reactive rate coefficient because once the complex is formed, it can either come back to the reactants C + NH_3 or evolve to form different products (H_2CN, cis-/trans-HCNH, or H_2NC).

According to the statistical RRKM theory, the microcanonical rate coefficient, K, leading to any possible product at a fixed collision energy, E, and total angular momentum, J, is expressed as (Marcus 1952a,b; Miller 1979, 1987)

$$K(E,J) = \frac{\sum_{v,K} P(E-\epsilon_{JKv})}{2\pi\hbar\rho(E,J)}, \quad (9)$$

where ϵ_{JKv} are the energies of the vibrational and rotational levels at the saddle point that yield each product, and $\rho(E,J)$ is the density of states of the initial system, which in our case is the intermediate CNH_3 (I_4). The function $P(E-\epsilon_{JKv})$ in Eq. (9) is the transmission probability over the ϵ_{JKv} barrier and can be calculated classically or semiclassically by considering tunneling through a mono-dimensional Eckart barrier, as proposed by Miller (1979, 1987).

The intermediate CNH_3 (I_4) will uni-molecularly decompose into three channels. The first is the re-dissociation back to the reactants C + NH_3 (R_2), over-passing the barrier of the effective $-A/R^4 + \hbar^2\ell(\ell+1)/2\mu R^2$ mono-dimensional potential (where ℓ is the orbital angular momentum of the C atom with respect to the center of mass of NH_3), similarly as is done in the capture model. The second channel leads to the products H + H_2NC (P_4) over-passing the TS_{I4P4} barrier. The third consists of a statistical mechanism in which TS_{I3I4} is over-passed to reach the I_3 intermediate. With this mechanism, the system will proceed toward I_2 and I_1 intermediates. This complex-forming mechanism is expected to behave statistically, favoring an exit toward the most stable product, H + H_2CN (P_1). This was the case calculated by Cimas & Largo (2006) in the N + CH_3 reaction. Here, we assumed as a zero-order approximation that once TS_{I3I4} is over-passed, the reaction mechanism yields only H + H_2CN (P_1).

The branching ratio between the two product channels leading to H_2NC (P_4) and H_2CN (P_1) is then given as a function of collision energy, E, as

$$\frac{[\mathrm{H_2NC}]}{[\mathrm{H_2CN}]}(E) = \frac{\sum_J (2J+1)K^{\mathrm{H_2NC}}(E,J)}{\sum_J (2J+1)K^{\mathrm{H_2CN}}(E,J)}. \quad (10)$$

The calculated branching ratio [H_2NC]/[H_2CN] is shown in Fig. 7 as a function of the collision energy using the CBS limit results from the RCCSD(T)-F12, MRCI-F12, and MRCI-F12+Q methods. It is seen that the branching ratio is very dependent on the relative heights of the barriers TS_{I4P4} and TS_{I3I4}, which in turn are very dependent on the method (i.e., on how electronic correlation is included). Saddle points correspond to the configurations where bonds are formed and destroyed, and hence,

multi-reference methods are in principle more accurate. For this reason, we consider the MRCI-F12 and MRCI-F12+Q results to be the most accurate in the present work. The inclusion of tunneling only accounts for corrections of about 2%. It is worth noting that the energy differences between the barriers TS_{I4P4} and TS_{I3I4} involved in this reaction are probably close to the accuracy of state-of-the-art ab initio methods. For all explored methods, the [H_2NC]/[H_2CN] branching ratio is almost constant for collision energies below ∼0.3 eV. Above this energy, the ratio increases because the density of states at TS_{I4P4} increases faster than at TS_{I3I4} due to the smaller rotational constants. Using the MRCI+Q-CBS results, the rotational constants for TS_{I4P4} are 5.18 cm^{-1}, 0.98 cm^{-1}, and 0.96 cm^{-1}, while for TS_{I3I4} they are 6.49 cm^{-1}, 0.87 cm^{-1}, and 0.86 cm^{-1}.

We can conclude that the [H_2NC]/[H_2CN] branching ratio at 10 K should have a value between 0.5 and 0.8. This value is to be compared with the abundance ratio H_2NC/H_2CN observed in cold dense clouds in this work, which lies between 0.51 and >2.7 (see Table 3). Taking into account the significant variation in the predicted branching ratio [H_2NC]/[H_2CN] with the method employed and the spread of H_2NC/H_2CN ratios found in the targeted clouds, the reaction C + NH_3 could be the main source of H_2NC in cold dense clouds, as well as in the redshifted galaxy in front of the quasar PKS 1830−211, where the abundance ratio H_2NC/H_2CN is 0.27.

6. Concluding remarks

We carried out an observational survey to search for the metastable isomer H_2NC toward various cold dense and diffuse clouds to determine its abundance and understand the chemistry of this recently discovered molecule. Simultaneously, the most stable isomer, H_2CN, was also searched for in the same sources. We were mainly interested in exploring two particular hypotheses suggested by the discovery of H_2NC. First, whether or not the H_2NC/H_2CN abundance ratio behaves like the HNC/HCN ratio, with values around one in cold dense clouds and below one in diffuse clouds. And second, whether or not H_2NC is chemically connected to ammonia.

We detected H_2NC in most of the cold dense clouds we targeted, which indicates that this species is widespread in this kind of interstellar cloud. On the other hand, we did not detect H_2NC or H_2CN toward the two diffuse clouds that seemed among the most favorable for detection, most likely because of the lower molecular richness of diffuse clouds compared to dense clouds. The non-detection of H_2NC toward diffuse clouds did not allow us to confirm the hypothesis that the H_2NC/H_2CN abundance ratio behaves similarly to the HNC/HCN in dense and diffuse clouds. On the other hand, we find that the column density of H_2NC is correlated with that of NH_3 because the sources where H_2NC is most abundant are also very abundant in ammonia. This fact suggests that these two molecules are chemically connected, probably because ammonia is a precursor of H_2NC through the C + NH_3 reaction.

Previous studies of the C + NH_3 reaction favored H_2CN as the main product. We thus revisited this reaction from a theoretical point of view and find that the two isomers H_2CN and H_2NC can be formed through two different reaction pathways that involve two different transition states, the energies of which are predicted to be very similar and slightly below that of the reactants. The product branching ratio H_2NC/H_2CN is predicted to be between 0.5 and 0.8. This is on the order of the abundance ratios H_2NC/H_2CN observationally found in cold dense clouds, which range from 0.51 to >2.7. We therefore conclude that the reaction C + NH_3 is probably the main formation route to H_2NC in interstellar clouds.

Acknowledgements. We acknowledge funding support from Spanish Ministerio de Ciencia e Innovación through grants PID2019-106110GB-I00, PID2019-107115GB-C21, PID2019-106235GB-I00, and PID2021-122549NB-C2. We thank the referee for useful comments that helped to improve this article.

References

Agúndez, M., Marcelino, N., Cernicharo, J. et al., 2019, A&A, 625, A147
Alves, T. V., de Oliveira Filho, A. G. S., & Ornellas, F. R. 2008, Chem. Phys. Lett., 457, 36
Anglada, G., Sepúlveda, I., & Gómez, J. F. 1997, A&AS, 121, 255
Benedettini, M., Pezzuto, S., Burton, M. G., et al. 2012, MNRAS, 419, 238
Benson, P. J., & Myers, P. C. 1989, ApJS, 71, 89
Bop, C. T., Batista-Romero, F. A., Faure, A., et al. 2019, ACS Earth Space Chem., 3, 1151
Bourgalais, J., Capron, M., Kailasanathan, R. K. A., et al. 2015, ApJ, 812, 106
Cabezas, C., Agúndez, M., Marcelino, N., et al. 2021, A&A, 654, A45
Chiba, S., Honda, T., Kondo, M., & Takayanagi, T. 2015, Comput. Theor. Chem., 1061, 46
Cimas, A. & Largo, A. 2006, J. Phys. Chem. A, 110, 10912
Corby, J. F., McGuire, B. A., Herbst, E., & Remijan, A. J. 2018, A&A, 610, A10
Cowles, D. C., Travers, M. J., Frueh, J. L., & Ellison, G. B. 1991, J. Chem. Phys., 94, 3517
Davidson, E. R. 1975, J. Comput. Phys., 17, 87
González, C., & Schlegel, H. B. 1992, J. Am. Chem. Soc., 114, 9118
Greaves, J. S., & Nyman, L.-Å. 1996, A&A, 305, 950
Greaves, J. S., White, G. J., Ohishi, M., et al. 1992, A&A, 260, 381
Henkel, C., Braatz, J. A., Menten, K. M., & Ott, J. 2008, A&A, 485, 451
Hernández Vera, M., Lique, F., Dumouchel, F., et al. 2017, MNRAS, 468, 1084
Hickson, K. M., Loison, J.-C., Bourgalais, J., et al. 2015, ApJ, 812, 107
Hirota, T., Yamamoto, S., Mikami, H., & Ohishi, M. 1998, ApJ, 503, 717
Huh, S. B., & Lee, J. S. 2003, J. Chem. Phys., 118, 3035
Lee, J. S., & Park, S. Y. 2000, J. Chem. Phys., 112, 10746
Lee, J., & Taylor, R. 1989, Int. J. Quantum Chem., 36, 199
Linke, R. A., Stark, A. A., & Frerking, M. A. 1981, ApJ, 243, 147
Liszt, H., & Lucas, R. 1995, A&A, 299, 847
Liszt, H., & Lucas, R. 2001, A&A, 370, 576
Liszt, H., Lucas, R., & Pety, J. 2006, A&A, 448, 253
Liszt, H., Pety, J., & Lucas, R. 2008, A&A, 486, 493
Marcus, R. A. 1952a, J. Chem. Phys., 20, 352
Marcus, R. A. 1952b, J. Chem. Phys., 20, 355
Marston, G., Nesbitt, F. L., Nava, D. F., et al. 1989a, J. Phys. Chem., 93, 5769
Marston, G., Nesbitt, F. L., & Stief, L. J. 1989b, J. Chem. Phys., 91, 3483
Mendes, M. B., Buhr, H., Berg, M. H., et al. 2012, ApJ, 746, L8
Miller, W. H. 1979, J. Am. Chem. Soc., 101, 6810
Miller, W. H. 1987, Chem. Rev., 87, 19
Muller, S., Beelen, A., Guélin, M., et al. 2011, A&A, 535, A103
Nyman, L.-Å, 1984, A&A, 141, 323
Ohishi, M., McGonagle, D., Irvine, W. M., et al. 1994, ApJ, 427, L51
Peterson, K. A., & Werner, H.-J. 2008, J. Chem. Phys., 128, 084102
Puzzarini, C. 2010, Int. J. Quantum Chem., 110, 2483
Sadygov, R. G., & Yarkony, D. R. 1997, J. Chem. Phys., 107, 4994
Sakai, N., Shiino, T., Hirota, T., et al. 2010, ApJ, 718, L49
Sarrasin, E., Ben Abdallah, D., Wernli, M., et al. 2010, MNRAS, 404, 518
Schilke, P., Keene, J., Le Bourlot, J., et al. 1995, A&A, 294, L17
Shiozaki, T., & Werner, H.-J. 2013, Mol. Phys., 111, 607
Stark, R., Wesselius, P. R., van Dishoeck, E. F., & Laureijs, R. J. 1996, A&A, 311, 282
Stief, L. J., Marston, G., Nava, D. F., et al. 1988, Chem. Phys. Lett., 147, 570
Suzuki, H., Yamamoto, S., Ohishi, M., et al. 1992, ApJ, 392, 551
Tercero, B., Cernicharo, J., Cuadrado, S., et al. 2020, A&A, 636, A7
Vastel, C., Loison, J.-C., Wakelam, V., & Lefloch, B. 2019, A&A, 625, A91
Velilla, L., Paniagua, M., & Aguado, A. 2010, Int. J. Quantum Chem., 111, 387
Werner, H.-J., & Knowles, P. J. 1989, J. Chem. Phys., 89, 5803
Werner, H.-J., Knowles, P. J., Knizia, G., et al. 2012, WIREs Comput. Mol. Sci., 2, 242
Yuen, C. H., Ayouz, M. A., Balucani, N., et al. 2019, MNRAS, 484, 659
Zeimen, W. B., Kłos, J., Groenenboom, G. C., & van der Avoird, A. 2003, J. Chem. Phys., 118, 7340